Mon. Not. R. Astron. Soc. **000**, 1–8 (2015) Printed 1 June 2016 (MN LaTeX style file v2.2)

NIHAO VII: Predictions for the galactic baryon budget in dwarf to Milky Way mass haloes

Liang Wang[1,3⋆], Aaron A. Dutton[2,3], Gregory S. Stinson[3], Andrea V. Macciò[2,3], Thales Gutcke[3], Xi Kang[1]
[1]*Purple Mountain Observatory, the Partner Group of MPI für Astronomie, 2 West Beijing Road, Nanjing 210008, China*
[2]*New York University Abu Dhabi, PO Box 129188, Abu Dhabi, UAE*
[3]*Max-Planck-Institut für Astronomie, Königstuhl 17, 69117 Heidelberg, Germany*

to be submitted to MNRAS

ABSTRACT
We use the NIHAO galaxy formation simulations to make predictions for the baryonic budget in present day galaxies ranging from dwarf ($M_{200} \sim 10^{10}\mathrm{M}_\odot$) to Milky Way ($M_{200} \sim 10^{12}\mathrm{M}_\odot$) masses. The sample is made of 88 independent high resolution cosmological zoom-in simulations. NIHAO galaxies reproduce key properties of observed galaxies, such as the stellar mass vs halo mass and cold gas vs stellar mass relations. Thus they make plausible predictions for the baryon budget. We present the mass fractions of stars, cold gas ($T < 10^4$K), cool gas ($10^4 < T < 10^5$K), warm-hot gas ($10^5 < T < 10^7$K), and hot gas (10^7K$< T$), inside the virial radius, R_{200}. Compared to the predicted baryon mass, using the dark halo mass and the universal baryon fraction, $f_\mathrm{b} \equiv \Omega_\mathrm{b}/\Omega_\mathrm{m} = 0.15$, we find that all of our haloes **are missing baryons. The missing mass been relocated past 2 virial radii, and is dominated by cool gas.** Haloes of mass $M_{200} \sim 10^{10}\mathrm{M}_\odot$ are missing $\sim 90\%$ of their baryons. More massive haloes ($M_{200} \sim 10^{12}\mathrm{M}_\odot$) retain a higher fraction of their baryons, with $\sim 30\%$ missing, consistent with observational estimates.

Key words: galaxies: evolution – galaxies: formation – galaxies: dwarf – galaxies: spiral – methods: numerical – cosmology: theory

1 INTRODUCTION

Cosmic structure formation has redistributed the baryons from a nearly uniformly distributed plasma into a variety of states, including stars, stellar remnants, cold (atomic and molecular) gas, and hot (ionized) gas. The theories of galaxy formation can predict the amount of mass in these different states, which can in turn be tested by observational constraints.

On cosmological scales, the ratio between the total baryonic and gravitating mass is measured to be $f_\mathrm{b} \equiv \Omega_\mathrm{b}/\Omega_\mathrm{m} \simeq 0.15$ (The Planck Collaboration 2014). However, the cold baryonic mass density implied by several galaxy baryon estimates is only 3-8% of the big bang nucleosynthesis expectation (Persic & Salucci 1992; Fukugita et al. 1998; Bell et al. 2003; McGaugh et al. 2010). The majority of the cosmic baryons are thought to be in the form of hot gas around or between galaxies (Cen & Ostriker 1999). Until recently only a fraction of these baryons had been detected (Bregman 2007; Shull et al. 2012). This discrepancy is referred to as the "missing baryon problem". **Several theoretical studies with cosmological simulations have constrained the phase and cosmological environments of the potential reservoirs of the missing baryons (Yoshida et al. 2005; He et al. 2005; Davé et al. 2010; Zhu et al. 2011; Haider et al. 2016).**

The circum galactic medium (CGM) is a major potential reservoir of the missing baryons. Recent advances in the detection of gas in the CGM have come from the COS survey (Tumlinson et al. 2011, 2013; Thom et al. 2012; Werk et al. 2012, 2013). On the scale of Milky Way mass haloes $M_{200} \sim 10^{12}\mathrm{M}_\odot$ a significant amount of warm ($10^4 < T < 10^7$K) gas has been detected (Werk et al. 2014), accounting for 33-88% of the baryon budget. In the future such observations will be extended to a wider range of halo masses. **The physical properties of the CGM has been shown to be able to test feedback models (Sharma et al. 2012; Marasco et al. 2013). Davé (2009) predicted galactic halo baryon fractions of galaxies with halo masses ranging from $10^{11}\mathrm{M}_\odot$ to $10^{13}\mathrm{M}_\odot$ using cosmological hydrodynamical simulations with a well-constrained model for galactic outflows. They found that, without the outflow model, the baryon fraction inside the virial radius is roughly the cosmic**

⋆ wangliang@pmo.ac.cn

baryonic fraction, but with the outflow model, the baryon fraction is increasingly suppressed in lower mass haloes. By comparing results at $z = 3$ and $z = 0$, they showed that large haloes remove their baryons at early times while small haloes lose baryons more recently due to the wind material taking longer to return to low-mass galaxies than high-mass galaxies. Sokolowska et al. (2016) studied the halo gas of three Milky way-sized galaxies using cosmological zoom-in simulations. They found that most of missing baryons actually resides in warm-hot and hot gas which contribute to 80% of the total gas reservoir. The recovered baryon fraction within 3 virial radii is 90%. The warm-hot medium is sensitive to the feedback model so that a reliable spatial mapping of the warm-hot medium will provide a stringent test for feedback models.

In this paper we make predictions for the baryonic budget for stars, cold, warm and hot gas in and around the virial radius of haloes of mass ranging from $M_{200} \sim 10^{10}\mathrm{M}_{\odot}$ to $10^{12}\mathrm{M}_{\odot}$. We use a sample of 88 zoom-in galaxy formation simulations from the NIHAO project. NIHAO galaxies are consistent with the stellar mass vs halo mass relations from halo abundance matching since redshift $z \sim 4$ (Wang et al. 2015), the galaxy star formation rate vs stellar mass relation since $z \sim 4$ (Wang et al. 2015), and the cold gas mass vs stellar mass relation at $z \sim 0$ (Stinson et al. 2015). Therefore, the simulations make plausible predictions for the mass fractions and physical locations of the warm and hot gas components. We find that all the haloes contain less baryons than expected according to the cosmic baryonic fraction, but the missing fraction is strongly mass dependent. **Mention Gutcke et al. 2016**

This paper is organized as follows: The cosmological hydrodynamical simulations including star formation and feedback are briefly described in §2; In §3 we present the results including the baryonic budget, baryon distribution, and a comparison with observations; §4 gives a summary of our results.

2 SIMULATIONS

In this study we use simulations from the NIHAO (Numerical Investigation of a Hundred Astrophysical Objects) project (Wang et al. 2015). The initial conditions are created to keep the same numerical resolution across the whole mass range with typically a million dark matter particles inside the virial radius of the target halo at redshift $z = 0$. The halos to be re-simulated at higher resolution with baryons have been extracted from 3 different pure N-body simulations with a box size of 60, 20 and 15 h^{-1} Mpc respectively. We adopted the latest compilation of cosmological parameters from the Planck satellite (the Planck Collaboration et al. 2014). More information on the collisionless parent simulations and sample selection can be found in Dutton & Macciò (2014) and Wang et al. (2015)

We use the SPH hydrodynamics code GASOLINE (Wadsley et al. 2004), with a revised treatment of hydrodynamics as described in Keller et al. (2014). The code includes a subgrid model for turbulent mixing of metal and energy (Wadsley et al. 2008), heating and cooling include photoelectric

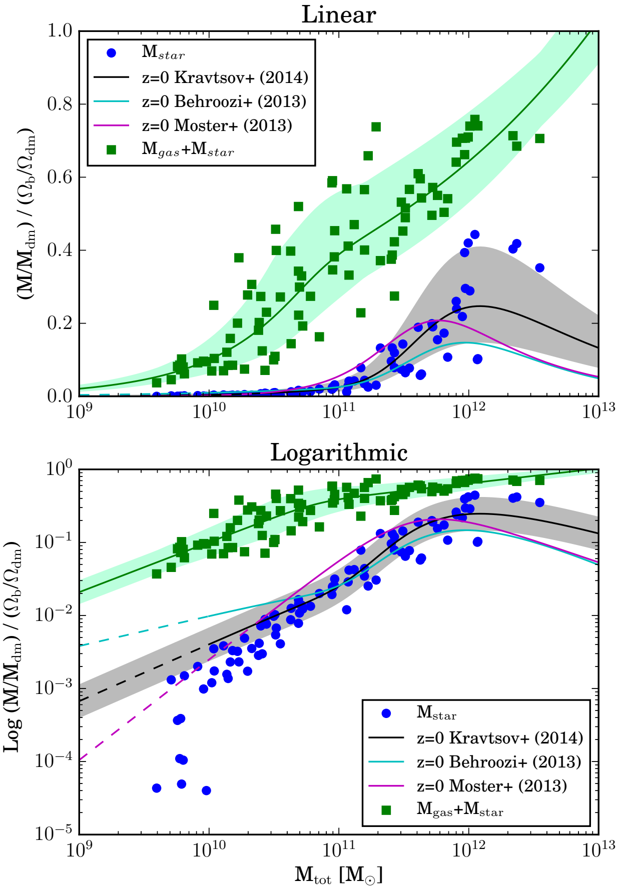

Figure 1. Fractional baryon content of our NIHAO simulations as a function of halo mass. The green points show the ratio between the baryonic mass (stars + gas) inside the virial radius and the total baryonic mass associated with the dark matter halo. The blue points show the corresponding fraction for the stars. The solid green line and shaded region shows a double power-law fit, together with the 1σ scatter. For the stellar mass fraction we show several relations from halo abundance matching. The linear (upper panel) and logarithmic (lower panel) scales emphasize the large amount of "missing" baryons and the low star formation efficiencies.

heating of dust grains, ultraviolet (UV) heating and ionization and cooling due to hydrogen, helium and metals (Shen et al. 2010). The star formation and feedback modeling follows what was used in the MaGICC simulations (Stinson et al. 2013). There are two small changes in NIHAO simulations: The change in number of neighbors and the new combination of softening length and particle mass increases the threshold for star formation from 9.3 to 10.3 cm^{-3}, the increase of pre-SN feedback efficiency $\epsilon_{\rm ESF}$, from 0.1 to 0.13. The more detail on star formation and feedback modeling can be found in Wang et al. (2015).

3 BARYON BUDGET

We define the fiducial baryonic mass as:

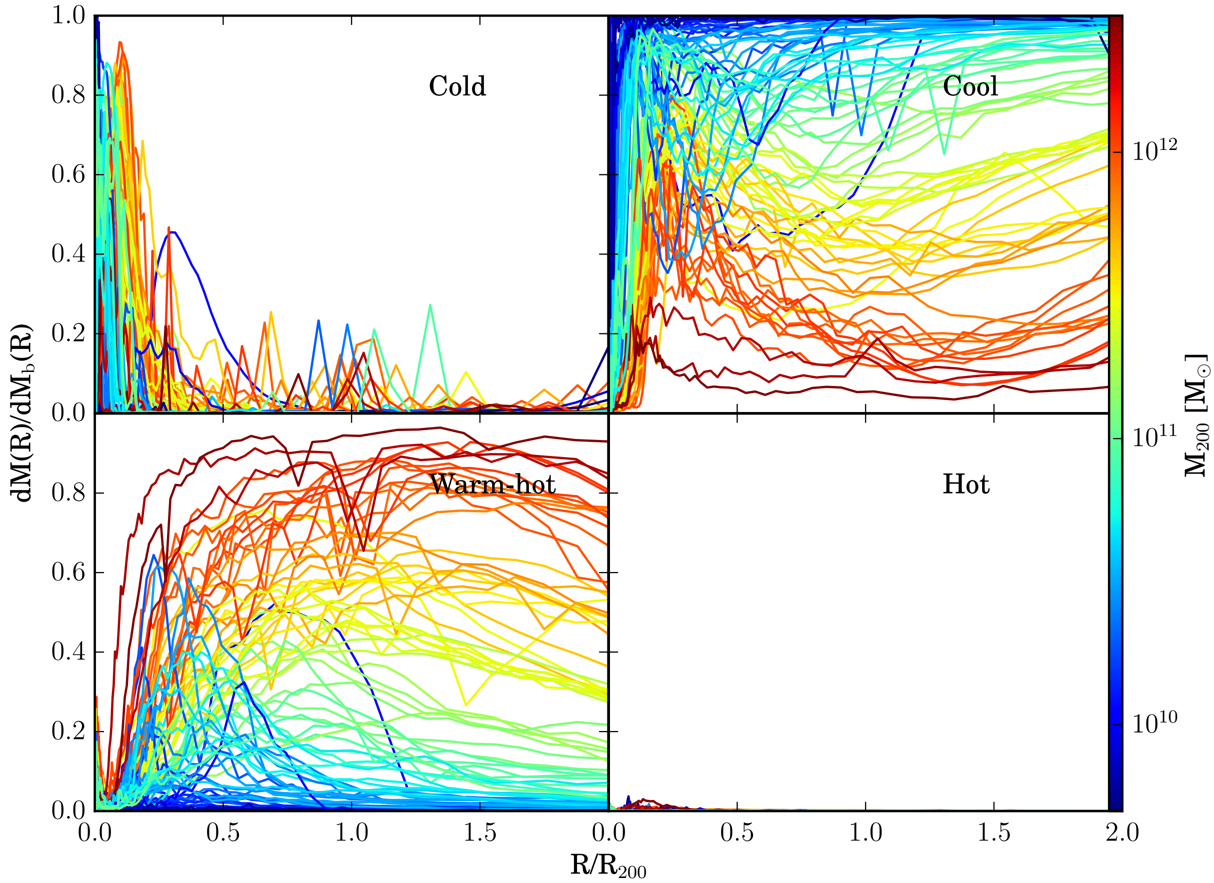

Figure 2. Radial profile of the mass fraction of the gas in each phase to total baryon mass in each radial bin at z=0 for all galaxies in NIHAO sample. Each solid line is from one galaxy and color coded with the halo mass. **tickmarks overlap. fix. use R_{200} for virial radius**

$$M_{\rm b} \equiv M_{\rm b}(R_{200}) = \frac{f_{\rm b}}{1-f_{\rm b}} M_{\rm dm}(R_{200}) \tag{1}$$

where the $M_{\rm dm}$ is the total dark matter mass in the halo, and the $f_{\rm b} = \Omega_{\rm b}/\Omega_{\rm m} \sim 0.15$ is the cosmic baryon fraction (the ratio between baryon density and mass density including baryonic mass plus dark matter), so that the $M_{\rm b}$ is the baryonic mass inside the virial radius if the baryons follow the dark matter closely.

Fig. 1 shows the ratio between the mass of each baryon component inside the virial radius to the fiducial baryonic mass for the most massive galaxy in each zoom-in region. We present the fractions of total stellar mass (blue points), and the total baryonic mass including stellar mass plus gas mass (green points). For the stellar mass fraction we also show the relations from the halo abundance matching (Moster et al. 2013; Behroozi et al. 2013; Kravtsov et al. 2014). The grey area is the one sigma scatter around the mean value from Kravtsov et al. (2014).

We tried to capture the behavior of the baryonic mass fraction as a function of the halo mass using a double power law formula:

$$\frac{f}{f_0} = \left(\frac{M_{200}}{\mathcal{M}_0}\right)^{\alpha} \left\{0.5\left[1+\left(\frac{M_{200}}{\mathcal{M}_0}\right)^{\gamma}\right]\right\}^{\frac{\beta-\alpha}{\gamma}} . \tag{2}$$

In this formula, the lower and higher mass ends have logarithmic slope α and β, respectively, while γ regulates how sharp the transition is from the lower to the higher ends. The best fit parameters are as follows:

$$\begin{aligned} \mathcal{M}_0 &= 6.76\times10^{10} \\ f_0 &= 0.336 \\ \alpha &= 0.684 \\ \beta &= 0.205 \\ \gamma &= 3.40 \end{aligned} \tag{3}$$

The green shaded region indicates the scatter about the best fit line, **which is 0.151 for haloes with mass in the range of $3\times10^9\mathrm{M}_\odot < \mathrm{M}_{200} < 2\times10^{10}\mathrm{M}_\odot$, 0.236 for halo mass in $2\times10^{10}\mathrm{M}_\odot < \mathrm{M}_{200} < 7\times10^{10}\mathrm{M}_\odot$, 0.125 for halo mass in $7\times10^{10}\mathrm{M}_\odot < \mathrm{M}_{200} < 3\times10^{11}\mathrm{M}_\odot$ and 0.0518 for halo mass in $3\times10^{11}\mathrm{M}_\odot < \mathrm{M}_{200} < 3.5\times10^{12}\mathrm{M}_\odot$.**

The trends of each component fraction are similar, in that the fractions are relatively low in low mass haloes, and increase as the halo mass increases. The main difference between the different components is the slope, with the baryonic mass fraction having a shallower slope than the stellar mass fraction. This is because in low mass haloes ($M_{200} \sim 10^{10}\mathrm{M}_\odot$) most of the baryons are in the form of gas, while in the highest mass haloes we study ($M_{200} \sim 10^{12}\mathrm{M}_\odot$) there are roughly equal amounts of stars and gas.

Fig. 1 shows that all haloes in our study contain less than the universal fraction of baryons. The upper panel uses a linear y-axis scale, which highlights the large amount of baryons that are missing, especially in low mass haloes. The logarithmic scale in the lower panel highlights the power-law nature of the relations.

Since the haloes we study are above the mass where the cosmic UV background prevents gas from cooling, the missing baryons have most likely been ejected from the central galaxies in supernova/stellar feedback driven winds. Although the lower mass galaxies have converted a smaller fraction of their available baryons into stars, and hence there is proportionally less energy available to drive an outflow, they have expelled a larger fraction of their baryons, consistent with expectations from energy driven gas outflows (e.g., Dutton 2012).

3.1 Mass budget of the corona

In Fig. 2, we present the radial distribution of gas in different phases at $z = 0$, normalized to the total baryon mass profile, such that for a given halo the four phases add up to unity. All simulations share a common attribute. The cold gas (T$< 10^4$ K) is mostly located near the center ($R < 0.2R_{200}$) where most stars in galaxies form. In contrast, the cool (10^4K $<$ T $< 10^5$K) and warm-hot (10^5K $<$ T $< 10^7$K) gas are located at large distances with roughly constant fractions up to 2 times R_{200}. The hot gas (T$> 10^7$K) is a minority component for all galaxies in the NIHAO sample, with the maximum hot gas fraction at any radius being less than 5%.

Despite these similarities, we find a considerably higher proportion of cool gas in lower mass galaxies ($\mathrm{M_{tot}} < 10^{11}\mathrm{M}_\odot$) in the whole corona region. For higher mass galaxies, warm-hot gas dominates the corona which signals higher efficiency of feedback. Even beyond the virial radius, the cool and warm-hot gas has similar features as the gas within virial radius which reveals the gas surrounding galaxies within large distance is the major reservoir of baryons.

3.2 Where are the missing baryons?

Fig. 3 shows the mass ratio profiles of total baryons for each simulation. Here the y-axis is the ratio between the baryonic to dark matter mass, $M_\mathrm{b}(< R)/M_\mathrm{dm}(< R)$, enclosed within a sphere of radius, R, normalized by the cosmic baryon-to-dark matter ratio, $\Omega_\mathrm{b}/\Omega_\mathrm{dm}$.

Each solid curve represents a halo, and the curves are colored by their halo mass (red for high masses to blue for low masses). Broadly speaking, the curves have a similar shape, with a normalization that depends on halo mass. They have a cusp in the central region where the stars and cold gas dominate, then become flat in the outer region. More massive haloes have higher baryon fractions at all radii. At small radii, the baryon to dark matter ratio is higher than the cosmic value due to gas dissipation. Even beyond the virial radius, there is little change in the baryon fraction up to 2 virial radii. We thus conclude that the missing baryons are well outside of the virial radius.

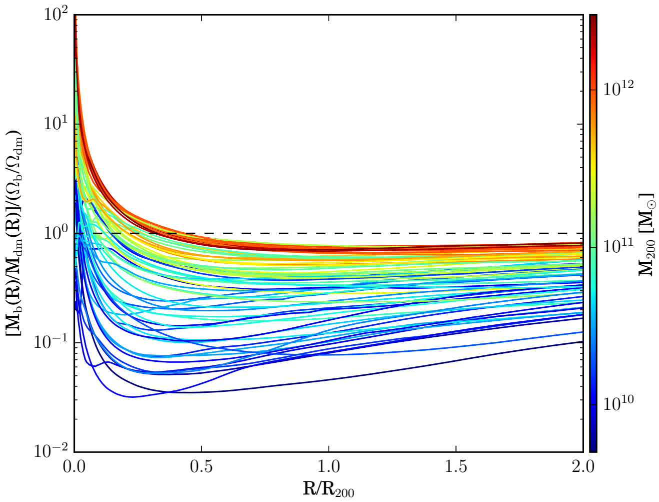

Figure 3. Baryon distribution of each galaxy from NIHAO simulations. The lines are color coded by their halo mass, which shows a clear trend that the more massive haloes preserve more baryons at all radii.

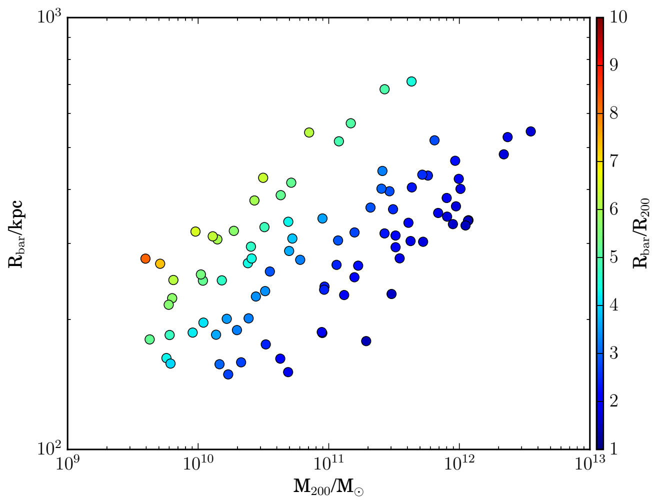

Figure 4. Baryon radius as function of total virial mass. The points are color coded by the ratio between baryon radius and the virial radius of each galaxy.

To estimate how far the baryons escape, we measured the radius, R_bar, within which the total baryon mass equals to the fiducial baryonic mass defined by Eq. 1. This is a lower limit to the true extent of the missing baryons since the baryon mass includes gas and stars that belong to nearby lower mass haloes. Fig. 4 shows the baryon radius of each galaxy as function of the virial mass. We find the baryon radius generally increases with virial mass.

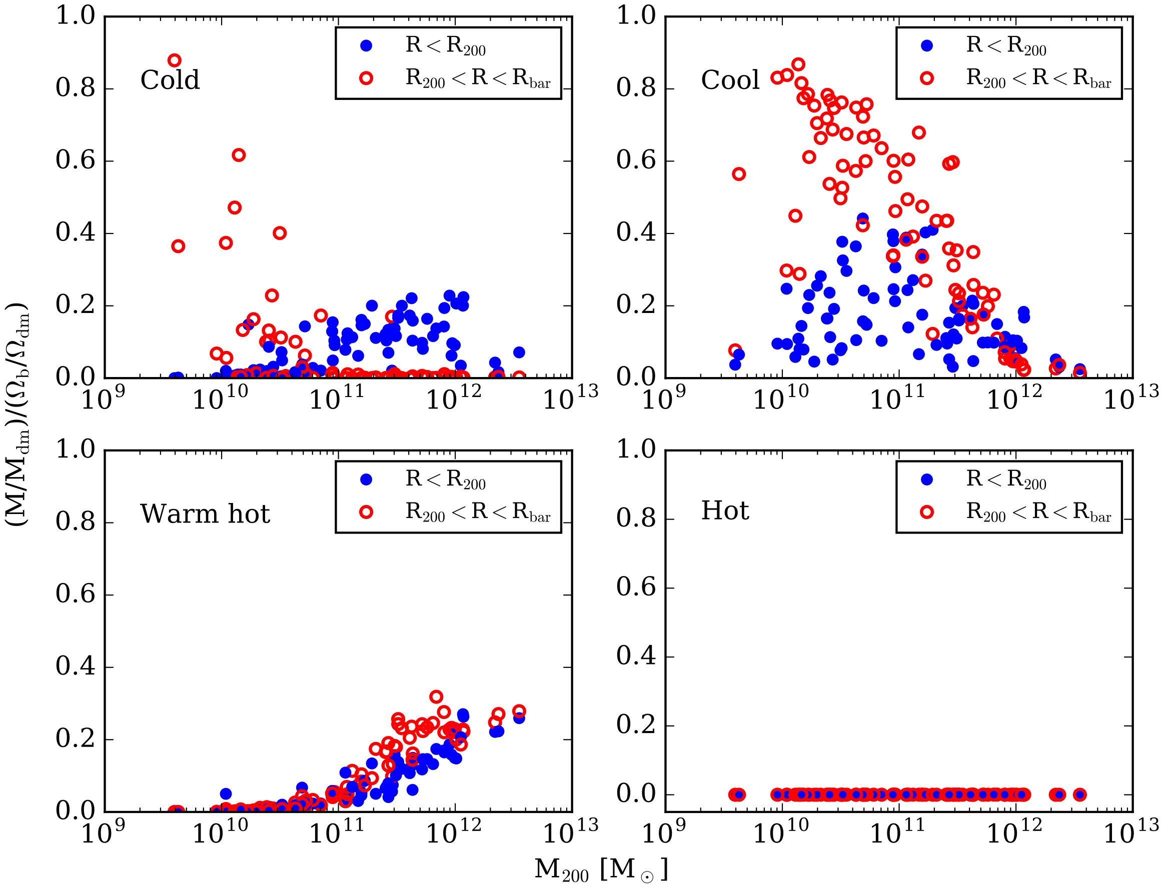

Figure 5. Mass fraction of gas in four phases (relative to the fiducial baryonic mass within virial radius). The blue and red points are for gas inside and outside the virial radius, respectively. Cool gas is the dominant component of the CGM in NIHAO simulations.

But when normalized by the virial radius, the distance baryons are ejected to span a similar range of radii $R_{\rm bar}/R_{200} \sim 2-6$.

In Fig. 5, we calculate the fractions of gas (in each phase) inside the virial radius (blue points) and between the virial and baryon radii (red points). The upper-left panel shows the fractions of cold gas. The fractions of cold gas between the virial radius and baryon radius of galaxies with halo masses in the range between $10^9 \rm M_\odot$ to $10^{10} \rm M_\odot$ are greater than 80%. As the halo mass increases, this fraction goes down dramatically, in the mass range between $10^{10} \rm M_\odot$ and $10^{11} \rm M_\odot$ the fractions are less than 20% for most of galaxies and the fractions for galaxies with halo mass above $10^{11} \rm M_\odot$ are almost 0. For the cold gas inside the virial radius, the fractions increase gradually as halo mass increases and the maximum fraction is about 20% with at a halo mass of $10^{12} \rm M_\odot$. The upper-right panel shows the fractions of cool gas. The fractions of cool gas in region outside of virial radius increase from 0 at halo masses are $10^9 \rm M_\odot$ to 80% at halo masses are around $10^{10} \rm M_\odot$ to $10^{11} \rm M_\odot$, then decrease in higher mass range and reach 0 again at halo masses are $10^{12} \rm M_\odot$. The cool gas inside virial radius shares a similar trend but the maximum fraction is about 40% at halo masses are $10^{11} \rm M_\odot$. The fractions for warm-hot gas are shown in the lower-left panel. The trends of the gas inside and outside gas are quite similar which increase as the halo masses increase monotonically and whose maximum values are only 20%. The hot gas shown in the lower-right panel and is negligible both inside and outside the virial radius across the whole mass range we study. We thus conclude that, for galaxies with halo mass below 10^{11}, the majority of baryons associated with the dark matter halo are in the cold and cool phases, and are located well outside of virial radius. For the gas inside virial radius, the majority is cool gas for the galaxies with halo masses are $10^{11} \rm M_\odot$ and when halo masses are higher than $10^{11} \rm M_\odot$ the fractions of cold gas, cool gas and warm-hot gas are comparable.

Table 1. The baryonic budget parameters for NIHAO galaxies in different halo mass bins. We refer to gas in the temperature range T $< 10^4$ K as cold; 10^4 K $\leqslant$ T $< 10^5$ K as cool; 10^5 K $\leqslant$ T $< 10^7$ K as warm; and T $\geqslant 10^7$ K as hot.

$\langle\log_{10}(M_{200}/\mathrm{M}_\odot)\rangle$	9.992 ± 0.223	10.588 ± 0.143	11.267 ± 0.209	11.963 ± 0.278
$\langle\log_{10}(M_\mathrm{b}/\mathrm{M}_\odot)\rangle$	9.243 ± 0.215	9.829 ± 0.139	10.493 ± 0.206	11.176 ± 0.273
$\langle M_\star/M_\mathrm{b}\rangle$	1.61×10^{-3}	9.57×10^{-3}	6.43×10^{-2}	0.240
$\sigma_\star$	1.63×10^{-3}	4.24×10^{-3}	5.02×10^{-2}	0.156
$\langle M_\mathrm{cold}/M_\mathrm{b}\rangle$	1.37×10^{-2}	3.92×10^{-2}	0.124	0.130
σ_cold	8.24×10^{-3}	4.08×10^{-2}	3.58×10^{-2}	7.78×10^{-2}
$\langle M_\mathrm{cool}/M_\mathrm{b}\rangle$	0.103	0.192	0.203	0.109
σ_cool	7.56×10^{-2}	0.135	0.138	6.37×10^{-2}
$\langle M_\mathrm{warm}/M_\mathrm{b}\rangle$	7.92×10^{-4}	1.48×10^{-2}	5.83×10^{-2}	0.167
σ_warm	1.25×10^{-3}	6.53×10^{-3}	3.19×10^{-2}	6.05×10^{-2}
$\langle M_\mathrm{hot}/M_\mathrm{b}\rangle$	0.000	0.000	0.000	1.82×10^{-4}
σ_hot	0.000	0.000	0.000	2.33×10^{-4}
$\left\langle M_\mathrm{missing}/M_\mathrm{b}\right\rangle$	0.880	0.744	0.548	0.350
σ_missing	5.65×10^{-2}	0.137	0.110	9.66×10^{-2}

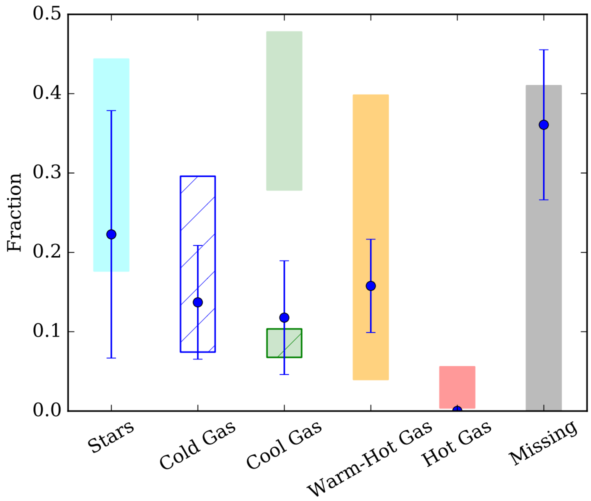

Figure 6. Baryonic budget of NIHAO haloes of mass $3.5\times10^{11} < M_{200}/\mathrm{M}_\odot < 3.5\times10^{12}$ (blue points with 1σ error bars) compared with observations of $M_{200} \sim 10^{12}\mathrm{M}_\odot$ haloes (shaded regions)

3.3 Comparison with Observations of Milky Way mass haloes

Since the CGM is too diffuse to create emission lines, it must be observed using quasar absorption lines. The COS-HALOs survey is filling in details about the $z \sim 0$ CGM (Peeples et al. 2014; Tumlinson et al. 2011, 2013; Werk et al. 2012, 2013, 2014). For the CGM of low-redshift $\sim L^*$ galaxies ($M_\mathrm{star} \sim 10^{10.5}\mathrm{M}_\odot$), Tumlinson et al. (2013) and Peeples et al. (2014) constrain the mass of the warm-hot CGM ($T \sim 10^{5-7}$K), Werk et al. (2014) provides a strict lower limit to the mass of cool material ($T \sim 10^{4-5}$K) in the CGM of these galaxies. In a study using X-rays, Anderson et al. (2013) place a constraints on the mass of hot gas ($T > 10^7$K) residing in the extended hot halos.

In Fig. 6, we show the mean values and standard deviation of the mass fraction of stars and different components of gas in our most massive galaxies ($3.49 \times 10^{11}\mathrm{M}_\odot < \mathrm{M}_{200} < 3.53 \times 10^{12}\mathrm{M}_\odot$) with blue points and error bars. The gas is assigned to a range of temperature bins: cold gas (T $< 10^4$ K), cool gas (10^4 K $<$ T $< 10^5$ K), warm gas (10^5 K $<$ T $< 10^7$ K) and hot gas (T $> 10^7$ K). The observational constraints are shown with the same colour scheme in Fig. 11 in Werk et al. (2014).

In this plot Werk et al. (2014) provides observational constraints for CGM gas mass that are shown as the shaded bars. The stellar mass range comes from halo abundance matching as described in Kravtsov et al. (2014). The cold disk gas mass comes from from Dutton et al. (2011).

The observations and the simulations match well in every phase **except** the cool CGM gas, where the observations find 3× the mass that simulations predict. If the observations are correct, the simulations have either ejected **cool gas too far**, or they have created a CGM with the wrong mix of gas temperatures. The total gas fractions (0.39 in COS-HALOs, 0.41 in NIHAO) suggest the latter option. **However, Stern et al. (2016) developed a new method to constrain the physical conditions in the cool CGM from measurements of ionic columns densities. This new method combines the information available from different sightlines during the photoionization modeling, and was applied to the COS-HALOs data, yielding a total cool CGM mass within the virial radius of $1.3 \times 10^{10}\mathrm{M}_\odot$ which is shown by the green hashed bar in Fig 1 and is in good agreement with our prediction. As the Fig. 2 and Fig. 5 show, the cool gas is the most important component in CGM so that the more accurate knowledge of the physical properties of CGM are necessary to better understand the role of the CGM in galaxy formation.** As the CGM of lower mass galaxies will soon be observed, Table 1 lists information about CGM mass fractions of the different components of gas in haloes down to a halo mass of $\sim 10^{10}\mathrm{M}_\odot$.

4 SUMMARY

We have used the NIHAO galaxy simulation suite (Wang et al. 2015) to study the statistical features of the baryonic budget and distribution spanning halo masses of $\sim 10^{10}$ to $\sim 10^{12}\mathrm{M}_\odot$. NIHAO is a large (currently 88) set of high resolution cosmological hydrodynamical galaxy formation simulations. As shown in previous papers the NIHAO galaxies reproduce several key observed scaling relations. We summarize our results as follows:

• All of the NIHAO haloes have a lower baryon to dark matter ratio, inside the virial radius, than the cosmic baryon fraction.

• **Cold gas ($T < 10^4$K) is mostly restricted to be within 0.2 virial radii. The cool gas ($10^4 < T < 10^5$K) dominates the corona at low masses ($M_{200} \lesssim 3 \times 10^{11}\mathrm{M}_\odot$) while the warm-hot gas ($10^5 < T < 10^7$K) dominates at high masses ($M_{200} \gtrsim 3 \times 10^{11}\mathrm{M}_\odot$).**

• The missing baryons in all haloes are beyond 2 virial radii.

• **Cool gas is a major component of the total baryons within $\mathrm{R}_{\mathrm{bar}}$, most of which is outside of the virial radius.**

• Lower mass haloes have lost a larger fraction of their baryons, even though they convert a lower fraction of the baryons into stars.

• For the highest mass haloes in our study $\sim 10^{12}\mathrm{M}_\odot$ our simulations are consistent with the observed fractions of stars, cold gas, warm and hot gas.

• **For the cool gas we predict $f_{\mathrm{cool}} = 0.11 \pm 0.06$ which is significantly lower than the observations from COS-HALOs ($f_{\mathrm{cool}} = 0.28 - 0.48$), but is in excellent agreement with the analysis of Stern et al. (2016).**

ACKNOWLEDGMENTS

Gasoline was written by Tom Quinn and James Wadsley. Without their contribution, this paper would have been impossible. The simulations were performed on the theo cluster of the Max-Planck-Institut für Astronomie and the hydra cluster at the Rechenzentrum in Garching; and the Milky Way supercomputer, funded by the Deutsche Forschungsgemeinschaft (DFG) through Collaborative Research Center (SFB 881) "The Milky Way System" (subproject Z2), hosted and co-funded by the Jülich Supercomputing Center (JSC). We greatly appreciate the contributions of all these computing allocations. AAD, GSS and AVM acknowledge support through the Sonderforschungsbereich SFB 881 The Milky Way System (subproject A1) of the German Research Foundation (DFG). The analysis made use of the pynbody package (Pontzen et al. 2013). The authors acknowledge support from the MPG-CAS through the partnership programme between the MPIA group lead by AVM and the PMO group lead by XK. LW acknowledges support of the MPG-CAS student programme. XK acknowledge the support from 973 program (No. 2015CB857003, 2013CB834900), NSFC project No.11333008 and the "Strategic Priority Research Program the Emergence of Cosmological Structures" of the CAS(No.XD09010000).

REFERENCES

Anderson, M. E., Bregman, J. N., Dai, X. 2013, ApJ, 762, 106
Agertz, O., Moore, B., Stadel, J. 2007, MNRAS, 380, 963
Behroozi, P. S., Wechsler, R. H., & Conroy, C. 2013, ApJ, 770, 57
Bell, E. F., McIntosh, D. H., Katz, N., Weinberg, M. D., 2003, ApJ, 585, 117
Bregman, J. N. 2007, ARAA, 45, 221
Cen, R. Y., Ostriker, J. P. 1999, ApJ, 514, 1
Davé, R. 2009, ASPC, 419, 347D
Davé, R., Oppenheimer, B. D., Katz, N., et al. 2010, MNRAS, 408, 2051
Dutton, A. A., Conroy, C., van den Bosch, F. C., et al. 2011, MNRAS, 416, 322
Dutton, A. A. 2012, MNRAS, 424, 3123
Dutton, A. A., & Macciò, A. V. 2014, MNRAS, 441, 3359
Fukugita, M., Hogan, C. J., Peebles, P. J. F. 1998, ApJ, 503, 518
Haider, M., Steinhauser, D., Vogelsberger, M., et al. 2016, MNRAS, 457, 3024
He, P., Feng, L. L., Fang, L. Z. 2005, ApJ, 623, 601
Keller, B. W., Wadsley, J., Benincasa, S. M., & Couchman, H. M. P. 2014, MNRAS, 442, 3013
Kravtsov, A., Vikhlinin, A., & Meshscheryakov, A. 2014, arXiv:1401.7329
Marasco, A., Marinacci, F., Fraternali, F. 2013, MNRAS, 433, 1634
McGaugh, S. S., Schombert, J. M., de Blok, W. J. G., Zagursky, M. J. 2010, MNRAS, 708, 14
Moster, B. P., Naab, T., & White, S. D. M. 2013, MNRAS, 428, 3121
Planck Collaboration, Ade, P. A. R., Aghanim, N., et al. 2014, A&A, 571, AA16
Peeples, M. S., Werk, J. K., Tumlinson, J., et al. 2014, ApJ, 786, 54
Persic, M., Salucci, P. 1992, MNRAS, 258, 14
Pontzen, A., Roškar, R., Stinson, G., & Woods, R. 2013, Astrophysics Source Code Library, 1305.002
Shen, S., Wadsley, J., & Stinson, G. 2010, MNRAS, 407, 1581
Sharma, P., McCourt, M., Parrish, I. J., Quataert, E. 2012, MNRAS, 427, 1219
Shull, J. M., Smith, B. D., Danforth, C. W. 2012, ApJ, 759, 23
Sokolowska, A., Mayer, L., Babul, A., Madau, P., Shen, S. 2016, ApJ, 819, 21
Stern, J., Hennawi, J. F., Prochaska, J. X., Werk, J. K. 2016, arXiv:1604.02168
Stinson, G. S., Brook, C., Macciò, A. V., et al. 2013, MNRAS, 428, 129
Stinson, G. S., Dutton, A. A., Wang, L., et al. 2015, MNRAS, 454, 1105
Thom, C., Tumlinson, J., Werk, J. K. 2012, ApJL, 758, L41
Tumlinson, J., Thom, C., Werk, J., et al. 2011, Science, 334, 948
Tumlinson, J., Thom, C., Werk, J., et al. 2013, ApJ, 777, 59
Wadsley, J. W., Stadel, J., & Quinn, T. 2004, NewA, 9, 137
Wadsley, J. W., Veeravalli, G., & Couchman, H. M. P. 2008, MNRAS, 387, 427
Wang, L., Dutton, A. A., Stinson, G. S., et al. 2015, MNRAS, 454, 83
Werk, J. k., Prochaska, J. X., Thom, C., et al. 2012, ApJS, 198, 3
Werk, J. k., Prochaska, J. X., Thom, C., et al. 2013, ApJS, 204, 17
Werk, J. k., Prochaska, J. X., Thom, C., et al. 2014, ApJ,

792, 8
Yoshida, N., Furlanetto, S. R., Hernquist, L. 2005, ApJ, 618L, 91
Zhu, W., Feng, L. L., Fang, L. Z. 2011, MNRAS, 415, 1093